nature geoscience

SUPPLEMENTARY INFORMATION

https://doi.org/10.1038/s41561-019-0458-8

In the format provided by the authors and unedited.

An interval of high salinity in ancient Gale crater lake on Mars

W. Rapin[1]*, B. L. Ehlmann[1,2], G. Dromart[3], J. Schieber[4], N. H. Thomas[1], W. W. Fischer[1], V. K. Fox[1], N. T. Stein[1], M. Nachon[5], B. C. Clark[6], L. C. Kah[7], L. Thompson[8], H. A. Meyer[1], T. S. J. Gabriel[9], C. Hardgrove[9], N. Mangold[10], F. Rivera-Hernandez[11], R. C. Wiens[12] and A. R. Vasavada[2]

[1]California Institute of Technology, Pasadena, CA, USA. [2]Jet Propulsion Laboratory, California Institute of Technology, Pasadena, CA, USA. [3]Laboratoire de Géologie de Lyon, Université de Lyon, Lyon, France. [4]Indiana University, Bloomington, IN, USA. [5]Texas A&M University, College Station, TX, USA. [6]Space Science Institute, Boulder, CO, USA. [7]University of Tennessee, Knoxville, TN, USA. [8]University of New Brunswick, Fredericton, Canada. [9]School of Earth and Space Exploration, Arizona State University, Tempe, AZ, USA. [10]Laboratoire de Planétologie et Géodynamique, UMR6112, CNRS, Université Nantes, Université Angers, Nantes, France. [11]Dartmouth College, Hanover, NH, USA. [12]Los Alamos National Laboratory, Los Alamos, NM, USA.
*e-mail: wrapin@caltech.edu

List of Figures and Tables:

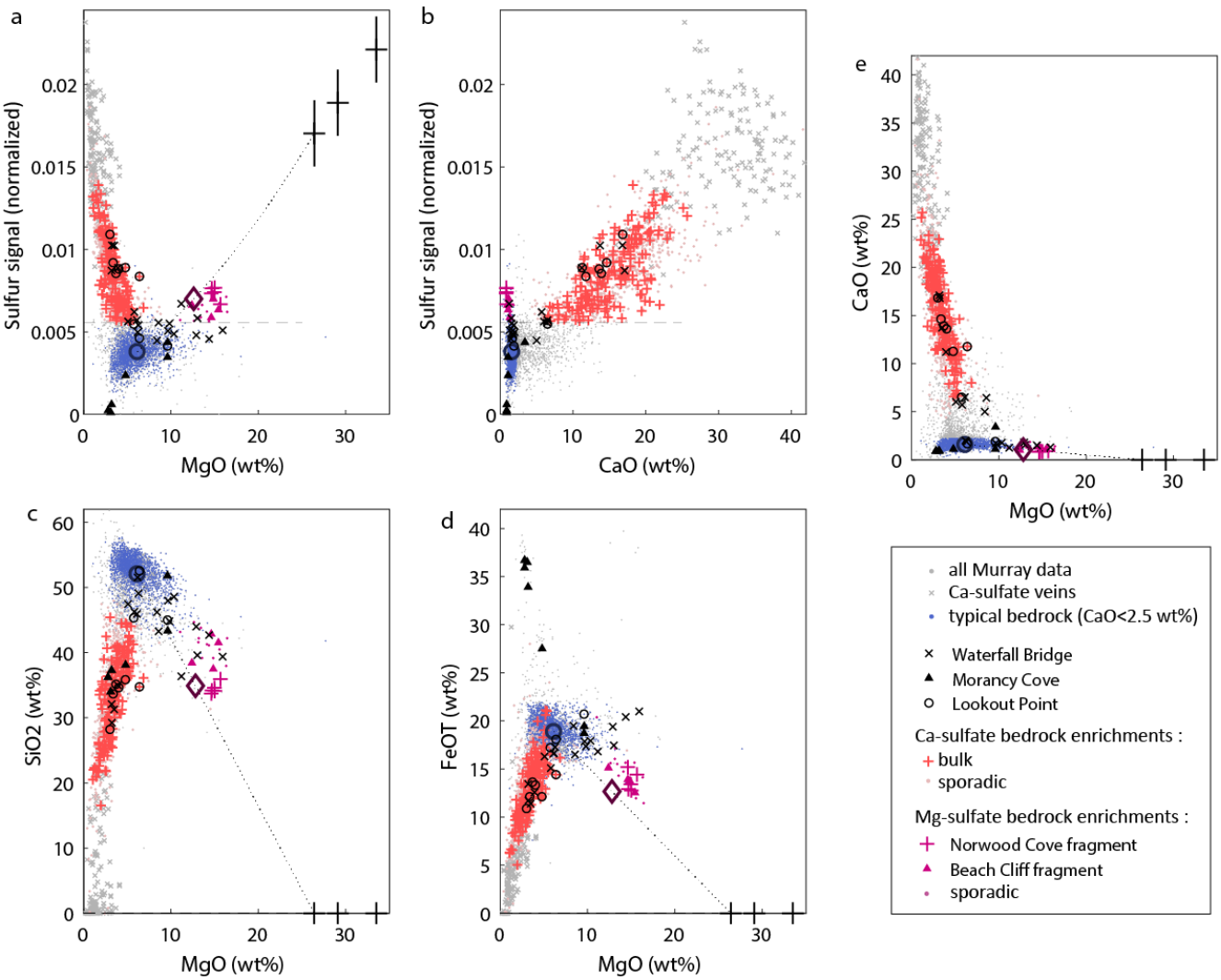

Figure S1: **ChemCam oxide and elemental data of the sulfate enrichments and other targets in the Murray formation.** Data from Figure 2 with: sulfur signal (peak area normalized to oxygen, see methods) (**a**), silica content (**c**), total iron oxide content (**d**), calcium oxide content (**e**) as a function of magnesium oxide content. Sulfur signal as function of CaO content is also shown (**b**). Additional targets include Morancy Cove, an iron rich feature (**d**); and Lookout Point, a Ca-sulfate enrichment in the bedrock (**b**, see Figure S4-a-c) observed in the vicinity of the Mg-sulfate enrichments. Ca-sulfate enrichments are also detected in target Waterfall Bridge at the location where small-scale white crystals have been observed (**b**, see Figure S4-g-j). This heterogeneous target includes points with Mg-sulfate detections as well distinct enhanced Fe and Mg points with low sulfur signal. In addition, all Murray bedrock data is shown with (grey) and without (blue) elevated CaO content (>2.5 wt%).

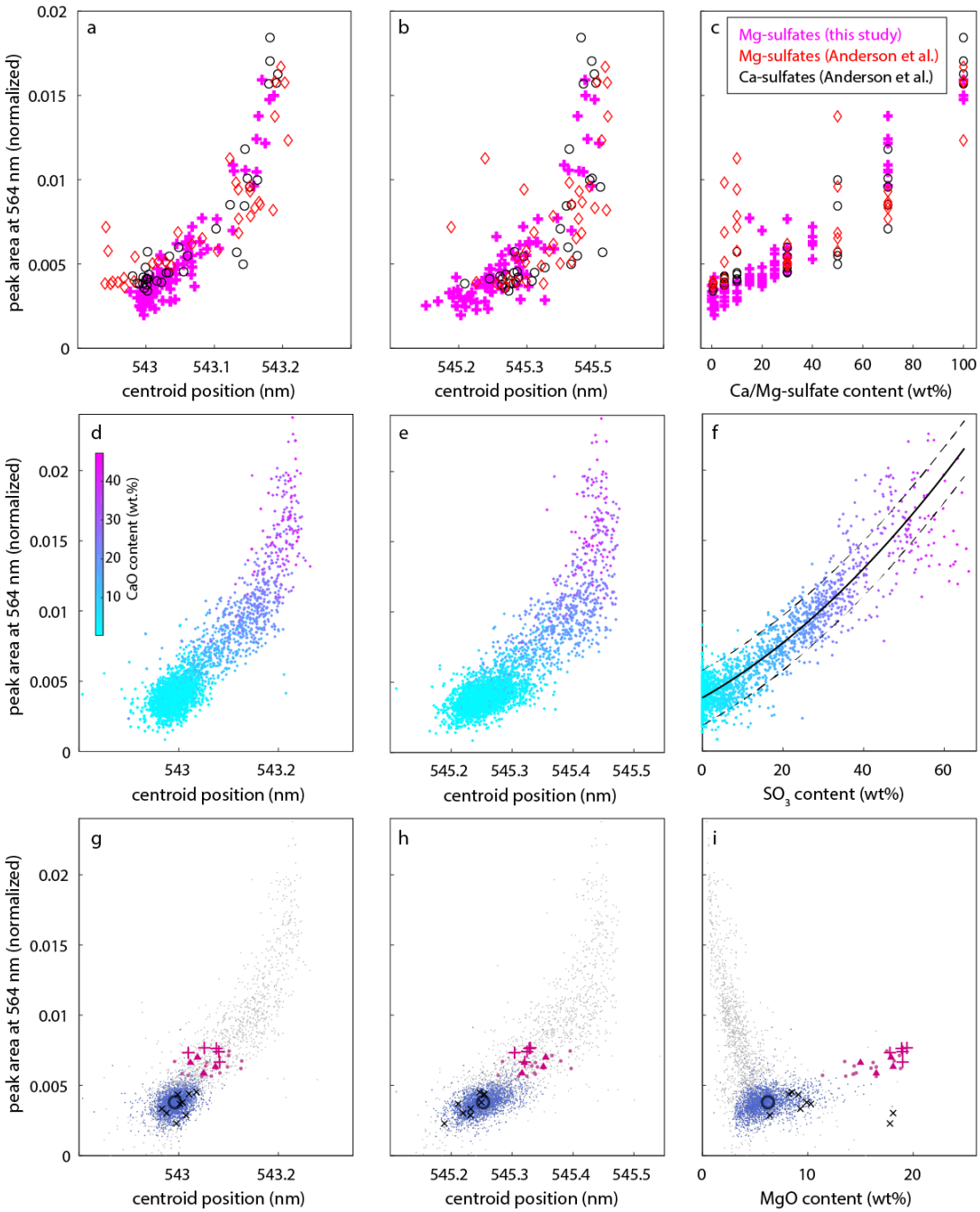

Figure S2: **Peak area and centroid position analysis for calibration of the sulfur signal.** Peak area at 564 nm (normalized to O I peak area at 778 nm), as a function of centroid position for the peak at ~543 nm (**a**), at ~546 nm (**b**), and Ca or Mg-sulfate content (**c**) of pellets analyzed at the laboratory (Table S3). Same parameters for spectra from Murray bedrock with large number of sporadic Ca-sulfate enrichments (**d-f**). **f**, calibration curve of the peak area as a function of inferred SO_3 content by Ca-sulfate contribution to the bedrock measured from CaO content, with 95% confidence bounds (dashed lines). The association of SO_3 to CaO enrichment is independently confirmed by APXS (Figure S3). **g-i**, Same data shown on Figure 2-b for Murray bedrock (blue) and Mg-sulfate enrichments (purple), and with additional: all bedrock observations including with Ca-sulfate enrichments (grey points and black arrow) and an igneous float rock (target name: Passagassawakeag, sol 1609) showing 2 of 9 points with elevated MgO content (**i**) not related to sulfur emission (dark crosses), as expected for ferromagnesian igneous minerals.

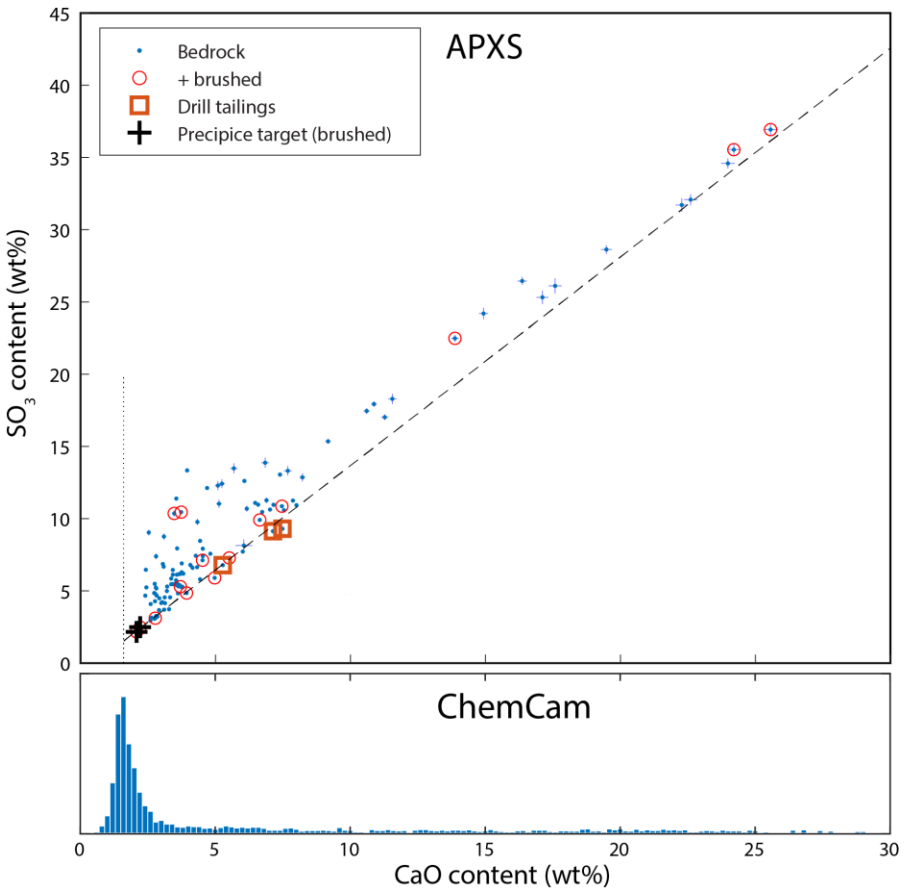

Figure S3: **APXS measurement of CaO and SO_3 content from Murray bedrock compared to ChemCam data on CaO content.** Ca and S oxides bulk centimeter scale content of Murray bedrock measured by APXS (footprint of ~17 mm) showing strong association up to 25 wt% CaO (top). The lowest bulk CaO and SO_3 content on Murray bedrock were measured on the Precipice target (black crosses). The target surface was brushed, so were a number of other Murray targets (red circles), to avoid contribution from sulfur-rich dust (Berger et al., 2016). The Murray bedrock measurements remain close or above the mixing trend between the Precipice target and the Ca-sulfate end-member (dashed line) which shows that all CaO enrichments likely correspond to a Ca-sulfate contribution. Error bars represent uncertainty on precision as reported in APXS calibrated data. The distribution of CaO contents measured at a submillimeter scale by the ChemCam instrument (bottom), shows most points on Murray bedrock group at CaO < 2.5 wt%, and a number of sporadic evenly distributed Ca-sulfate enrichments are observed at higher CaO contents. The average CaO content of 1.6 wt% for the low Ca Murray bedrock measured by ChemCam is marked with a vertical dotted line. It intercepts the mixing trend with Ca-sulfate at 1.5 wt% SO_3 content which therefore represents the amount of sulfate present in the Murray bedrock at a fine scale, possibly not attributed to Ca-sulfate.

Target name	Sol	Elevation	CaO content average (wt%)	CaO content standard deviation (wt%)	Number of points enriched	Bedrock target type
aegis_post_1472a	1472	-4372.61	14.9	4.7	4/9	mudstone
Mulondo	1473	-4372.21	8.8	2.5	5/10	sandstone
Tutume	1487	-4361.02	19.7	2.2	4/5	mudstone
Musserra	1492	-4360.91	13.4	1.4	4/5	mudstone
The_Bowl	1501	-4358.58	20.9	1.8	3/5	mudstone
Sutton_Island_ccam	1523	-4336.05	15.6	6.8	8/10	sandstone
Islesford	1523	-4335.94	14.5	3.5	5/5	sandstone
Duck_Harbor	1523	-4335.94	10.6	3.0	6/10	sandstone
Goose_Cove	1568	-4335.78	17.5	2.8	9/10	sandstone
aegis_post_1605a	1605	-4313.47	20.4	4.0	8/9	sandstone
Allagash	1626	-4306.45	12.8	3.5	5/9	mudstone
Deer_Isle_ccam	1671	-4296.24	22.3	1.1	4/5	mudstone
aegis_post_1673a	1673	-4294.55	13.1	2.1	7/9	mudstone
Lookout_Point	1674	-4294.45	15.6	2.7	6/9	mudstone
Carter_Cove	1684	-4284.21	20.8	2.1	7/10	sandstone
aegis_post_1693a	1693	-4279.34	18.8	1.6	5/9	mudstone
Fern_Spring	1703	-4270.07	24.9	3.3	10/10	mudstone
Redfield_Hill	1702	-4269.96	21.7	5.1	10/10	mudstone
aegis_post_1703a	1703	-4269.44	19.9	1.3	9/9	mudstone
White_Ledge_ccam	1710	-4267.14	14.7	2.1	8/10	sandstone
Shooting_Ledge	1710	-4267.05	15.1	1.8	6/10	sandstone
Ravens_Nest	1712	-4266	17.1	2.7	5/10	sandstone
McNeil_Point	1714	-4264.97	12.0	3.4	5/10	sandstone
Timber_Point_ccam	1715	-4264.87	12.2	1.5	4/9	sandstone
Spectacle_Island	1716	-4264.75	18.7	5.6	7/10	sandstone
aegis_post_1719a	1719	-4260.21	20.4	2.0	9/9	mudstone
aegis_post_1741a	1741	-4243.22	13.8	2.2	4/9	mudstone

Table S1: **List of ChemCam targets with Ca-sulfate bedrock enrichments.** Targets ordered by increasing elevation, with average and standard deviation of the CaO content of points with Ca-sulfate enrichment, i.e. CaO > 5 wt% and sulfur signal above the limit of detection. The number of enriched points on each target is also indicated against the number of point acquired. The bedrock type of the target, i.e. mudstone or sandstone is indicated based on visible grain-size and texture on RMI images, and MAHLI close-up images when available.

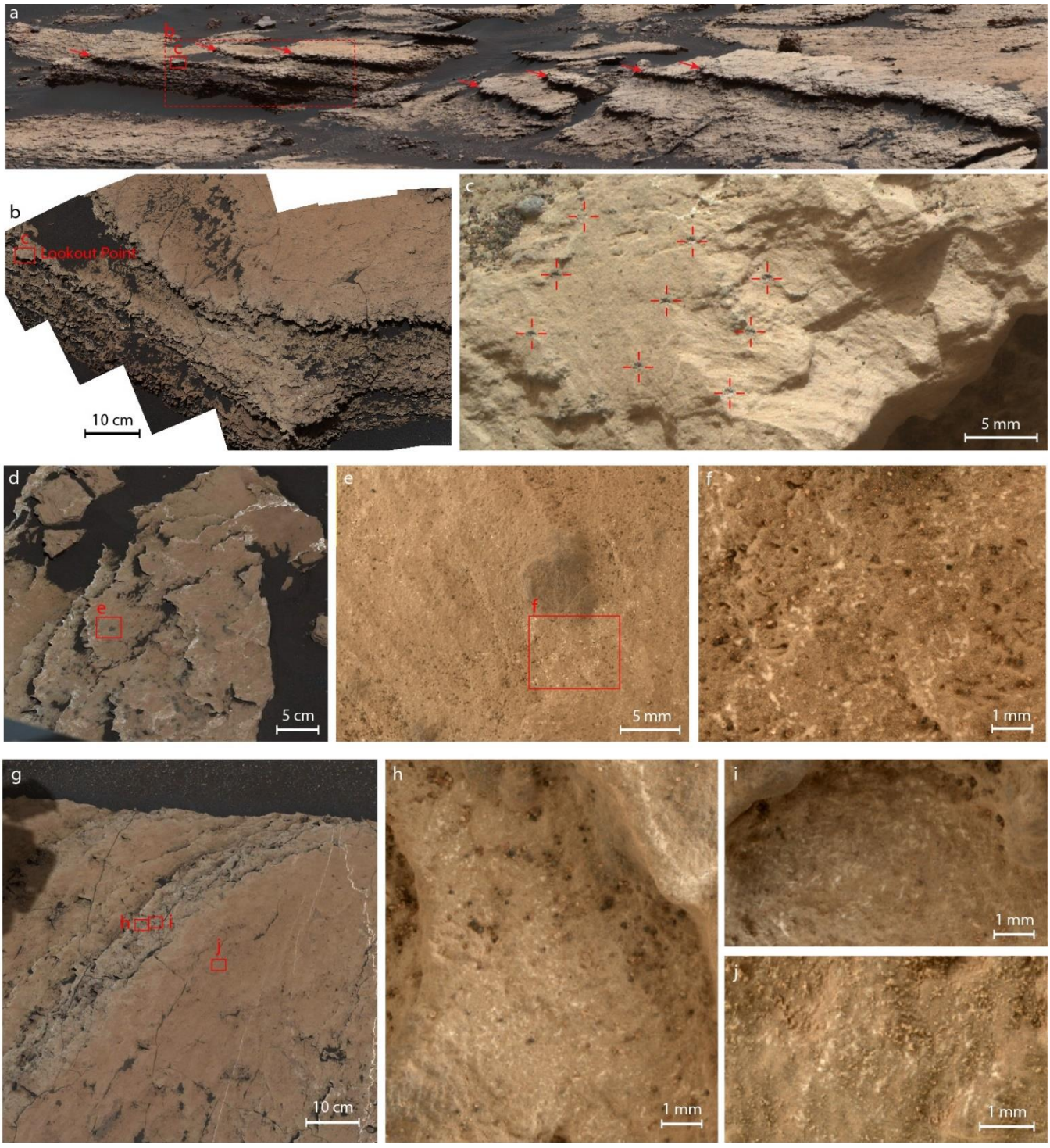

Figure S4: **Examples of Ca-sulfate enrichments observed within or close to the interval characterized by the Mg-sulfate enrichments**. Ca-sulfate enrichments observed in the form of erosion resistant horizons sol 1675 (red arrows) (**a**, mcam08669; **b**, mcam08693; **c**, 1675MH0001630000603488R00_DXXX), and small-scale white euhedral crystals spread within the bedrock on sol 1679 (**d**, mcam08712; **e**, 1679MH0001930000603557R00; **f**, 1679MH0001930000603555R00), as well as sol 1681 (**g**, mcam08726; **h-j**, 1682MH0001700000603651R00) see chemical data of the Waterfall Bridge target acquired at this location Figure S1.

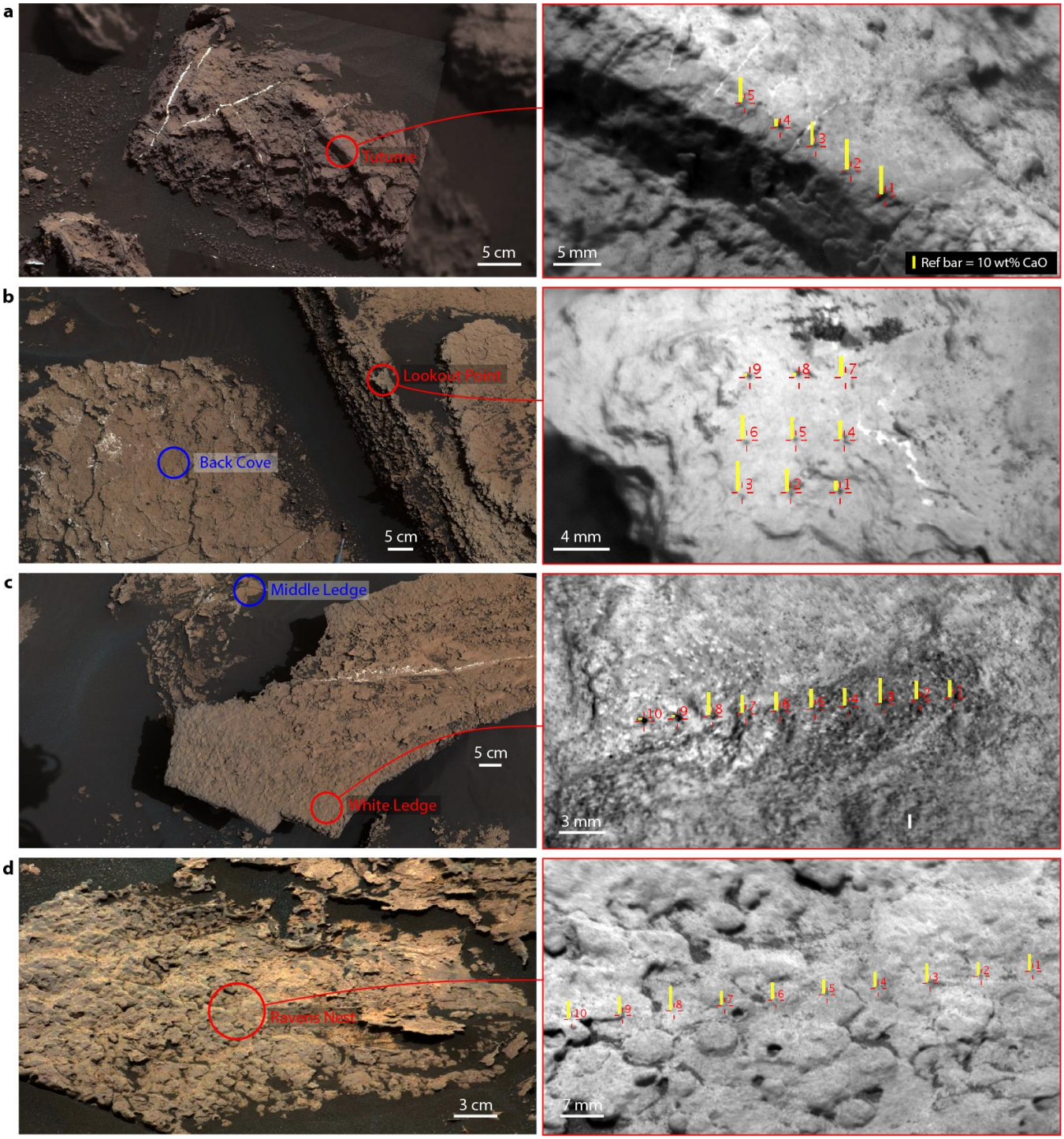

Figure S5: **Examples of Ca-sulfate enrichments with context and micro imagery. Left**, Mastcam color imaging of outcrops where targets with bedrock Ca-sulfate enrichments were analyzed by the ChemCam instrument (red circles) and other targets with typical Murray bedrock composition (CaO ~ 1.6 wt%) when available in the vicinity (blue circles). **Right**, Remote Micro Image (RMI) with location of the LIBS shots (red reticles) and annotated with yellow bars representing the CaO content for each point. **a**, MR_mcam07473, CCAM02487 Tutume; **b**, ML_mcam08680, CCAM02674 Lookout_Point; **c**, ML_mcam08906, CCAM01709 White_Ledge_ccam; **d**, MR_mcam08929, CCAM02712 Ravens_Nest.

Hydrated Mg-sulfate content estimation:

The hydrated Mg-sulfate content can be estimated on the Norwood Cove target assuming a binary mixture between an average bedrock composition and an Mg-sulfate end-member. It is calculated assuming extra MgO, SO_3 and water content compared to average bedrock composition can be attributed to a hydrated $MgSO_4$ end-member. The average sulfur signal of the bedrock is below ChemCam's detection limit (Figure 2). APXS measurements shows the bedrock (towards the lowest CaO content) is depleted in SO_3. According to the CaO-SO_3 correlation approximately 1.5 wt% SO_3 can be attributed to the low-CaO bedrock as measured by ChemCam (Figure S3). It should be noted that the Norwood Cove fragment has low CaO content (<1 wt%) highlighting that no significant Ca-sulfate could be contributing to its composition. The water content of the bedrock is estimated to 1.6 ± 0.4 wt% using ChemCam hydrogen signal (Rapin et al., 2017). Mg-sulfates are hygroscopic but their hydration state as an amorphous phase may vary widely; it is assumed that all the extra water content is attributed to the Mg-sulfate in the binary mixture model. The calculation for the Norwood Cove target resulted in up to 32.9 wt% hydrated Mg-sulfate, with 21.3 wt% water in the sulfate phase (table S2). Cases assuming SO_3 content at upper and lower limit on the 1-sigma uncertainty have been calculated as well because the sulfate quantification is the major source of uncertainty to define the Mg-sulfate content in the mixture model. Sulfate content close to the lower limit on uncertainty defines a lower limit on the hydrated Mg-sulfate content at 25.6 wt%. In the case of SO_3 content close to upper limit, MgO is the limiting oxide to define the amount of Mg-sulfate, resulting in residual SO_3 in the target.

		Norwood Cove fragment										bedrock
		#1	#2	#3	#4	#5	diff.	RMSE	avg.	min. SO_3	max. SO_3	avg.
Major Oxide Comp.	SiO_2	35.9	34.2	34.1	33.7	34.7	4%	12%	34.5	36.8	32.6	52.7
	TiO_2	0.7	0.7	0.6	0.8	0.8	9%	52%	0.7	0.8	0.7	1.0
	Al_2O_3	7.1	6.3	6.2	6.8	6.8	7%	41%	6.6	7.1	6.3	12.0
	FeO_T	14.4	12.9	12.8	15.2	13.4	11%	21%	13.7	14.6	13.0	19.0
	MgO	15.6	14.7	15.0	14.6	15.0	4%	22%	**15.0**	16.0	14.2	**6.4**
	CaO	0.9	0.9	0.9	0.8	0.9	5%	83%	0.9	0.9	0.8	1.6
	Na_2O	1.3	1.3	1.2	1.6	1.4	16%	37%	1.4	1.5	1.3	2.7
	K_2O	0.3	0.3	0.3	0.3	0.3	6%	178%	0.3	0.3	0.3	1.2
H calib.	H_2O	8.5	9.1	9.2	7.9	8.2	8%	22%	8.6	8.6	8.6	1.6
S calib.	SO_3	15.3	19.7	19.8	18.3	18.6	17%	32%	**18.4**	13.6	22.4	1.5
totals		100	100	100	100	100			100	100	100	99.7
hydrated Mg-sulfate content		29.9	37.1	37.4	33.8	34.5			**32.9**	25.6	35.6	
Mg-sulfate water content		23.1	20.2	20.3	18.6	19.1			**21.3**	27.3	19.6	
residual SO_3									0	0	3.3	
residual MgO		3.4	0.7	1.0	1.1	1.4			2.0	4.9	0	

Table S2: **Oxide content and modeled composition for the Mg-sulfate enriched fragment Norwood Cove.** Composition of the Norwood Cove target as measured by ChemCam after renormalization to account for sulfate and water content. The composition is reported for each of the 5 points raster (#1-#5), along with the maximum difference to the average (diff.) in percent, and the root mean square error on prediction from the calibration (RMSE) re-calculated as a percent of the average of the 5 points (not as wt%). RMSE for major oxides is obtained from calibration as described by Clegg et al. (2017), for water content by Rapin et al. (2017), and for sulfate content according to methods presented in this study (Figure S2). This shows that for all oxides the variability within the 5 points is well within uncertainty of prediction, highlighting homogeneity of the target. The average composition is reported on SO_3 content at $18.4^{+4.0}_{-4.8}$ wt% (avg.) with 1-sigma lower limit (min. SO_3), and upper limit (max. SO_3). For reference the average Murray bedrock composition is reported as well (bedrock avg.).

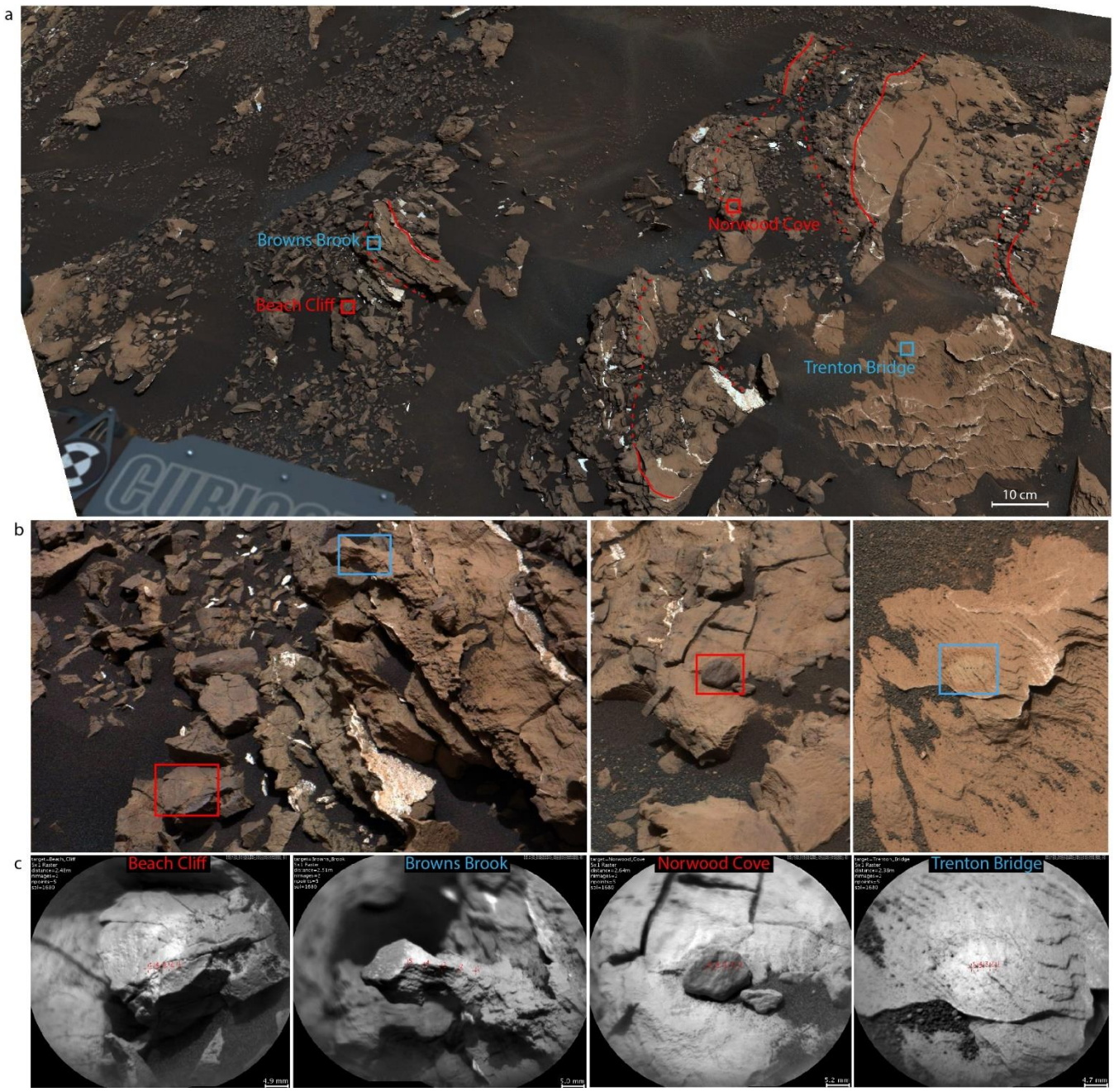

Figure S6: **ChemCam targets sampling the Mg-sulfate enriched lithology. a**, MastCam image mosaic of the bedrock in front of the rover, with red dashed lines marking boundaries between bedded dark-toned Mg-sulfate enriched lithology and interbedded typical Murray bedrock. Solid and dashed lines highlight sharp and approximate boundaries between the dark-toned Mg-sulfate enriched lithology and interbedded Murray bedrock. Location of the ChemCam LIBS analyses at this site are represented: Norwood Cove and Beach Cliff are Mg-sulfate enriched fragments (red rectangles), Trenton Bridge and Brown Brook sampled typical Murray bedrock (blue rectangles). **b**, Mastcam M100 context images of the ChemCam targets, rectangles highlight again the area of LIBS analyses. **c**, RMI mosaics of the ChemCam targets with annotated location of the LIBS measurement points (red reticles).

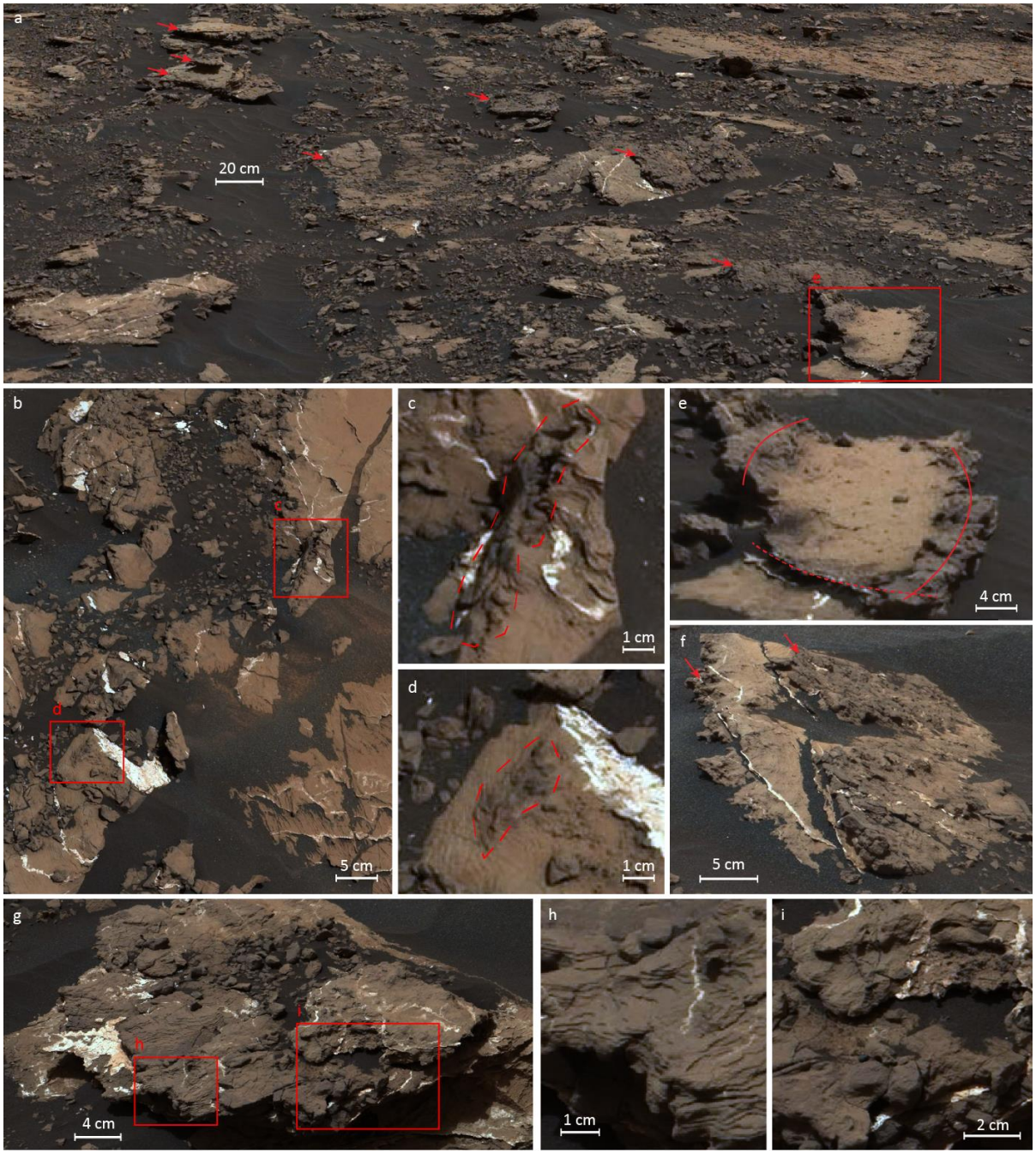

Figure S7: **Examples of Mg-sulfate enriched lithology observed on MastCam images. a**, Fields of centimeter-sized chunks lying over dark dune sand, relatively resistant to erosion, remnants of the lithology observed in the larger blocks of bedrock (red arrows), sol 1677 drive direction mosaic (mcam08703). **b**, Mastcam mosaic showing (see Figure S6) with close-ups **c** and **d** (red rectangles) for possible Mg-sulfate enriched nodules cross-cutting bedrock fine laminations at centimeter scale. **e**, Lateral texture variations forming ridges (solid and dashed red lines) (sol 1677 drive direction mosaic mcam08703) **e**, Lateral texture variations forming ridges (solid and dashed red lines) (sol 1677 drive direction mosaic mcam08703). **f**, Centimeter-thick beds (red arrows) with interbedded typical finely laminated Murray bedrock, sol 1678 Doubletop Mountain mosaic (mcam08708). **g**, reddish-brown block showing different textures occurring on the same block cross-cut by light-toned veins: **h**, coalescent nodular texture and **i**, in some cases preserved laminated texture, close-ups from sol 1678 Breaking Point mosaic (mcam08708).

Grain size sampling model for the Mg-sulfate enrichment:

A simulation model was run to evaluate the possible grain size of the Mg-sulfate and bedrock mixture observed on the Norwood Cove target. According to the oxide composition measured, the MgO and SiO_2 content on the 5 points, remain within 5% of the mean value (Table S2). A simulation was developed to determine the probability of 5 points to remain within the 5% interval as a function of grain size of the target. Sampling of the simulation is performed on an image of binary pixels representing clastic grains in a sedimentary rock (black) with space for cement between grains at 30% of the whole image (white) (Figure S8-a). A circle represents the sampled area. For each sampling, it is placed randomly on the image and the fraction of cement area (white space) within the circle is computed. The size of the circle (d_{LIBS}) relative to the volume mean diameter (D[4,3]) of the grain distribution (d_{grains}) on the image defines the scale of sampling relative to the simulated grain size. The d_{LIBS} value is defined by the ChemCam laser pit size estimated at 450 µm (at 2.6 m distance for the Norwood Cove target) as measured on Mars (Maurice et al., 2016). A simulation was run for grain sizes from 0.02 to 1 d_{LIBS} to compute for each grain size the probability of obtaining 5 points all within ± 5% of the mean 0.3 fraction of cement (Figure S8), as observed from the homogeneity of the 5 points raster on the Norwood Cove target (Table S2). This simulation shows that for the mixture model with grains and cement, the grain size observed at Norwood Cove is most likely silt because the probability to obtain the observed raster homogeneity with sand sizes is < 0.05.

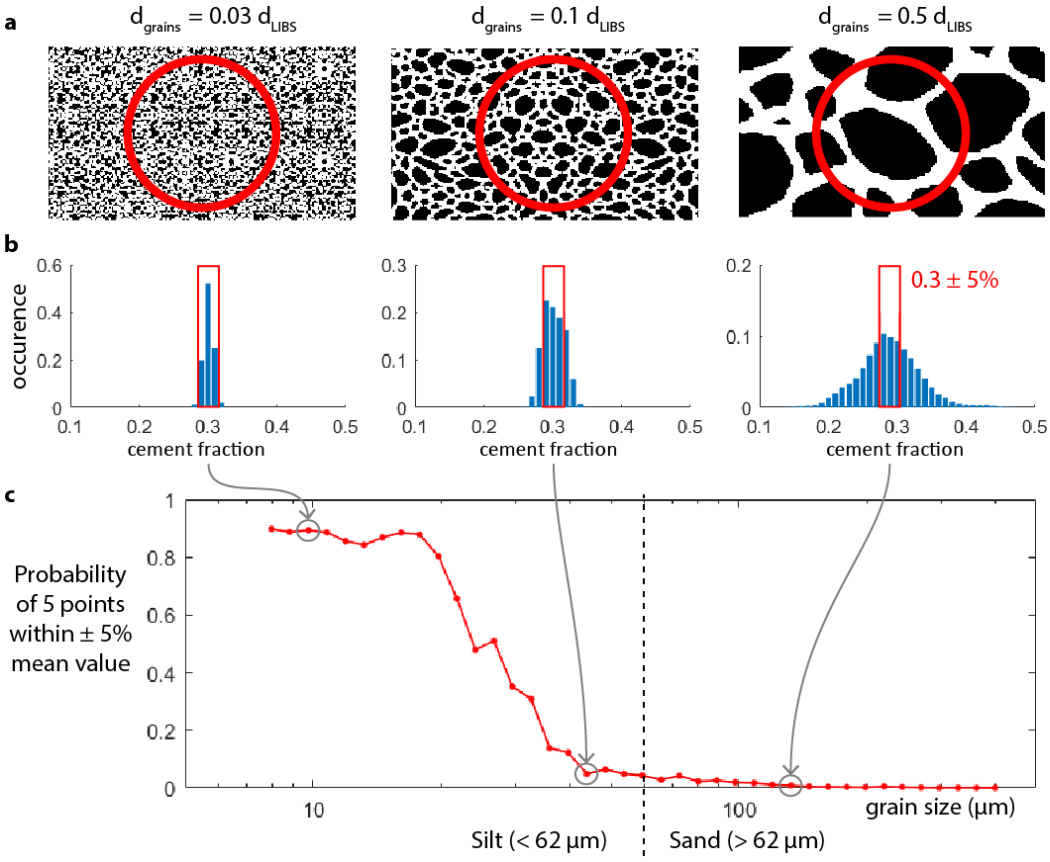

Figure S8: **Grain size sampling model. a**, examples of images generated with ChemCam sampling (red circle, diameter d_{LIBS}) on grains of various size (black, volume mean diameter d_{grains}) with 30% interstitial cement (white). **b**, distribution of cement fraction calculated from 100,000 random sampling, with homogeneity observed on the Norwood Cove target overlaid (red rectangle). **c**, calculated probability to obtain 5 points within 5% of the mean value for each grain size simulated.

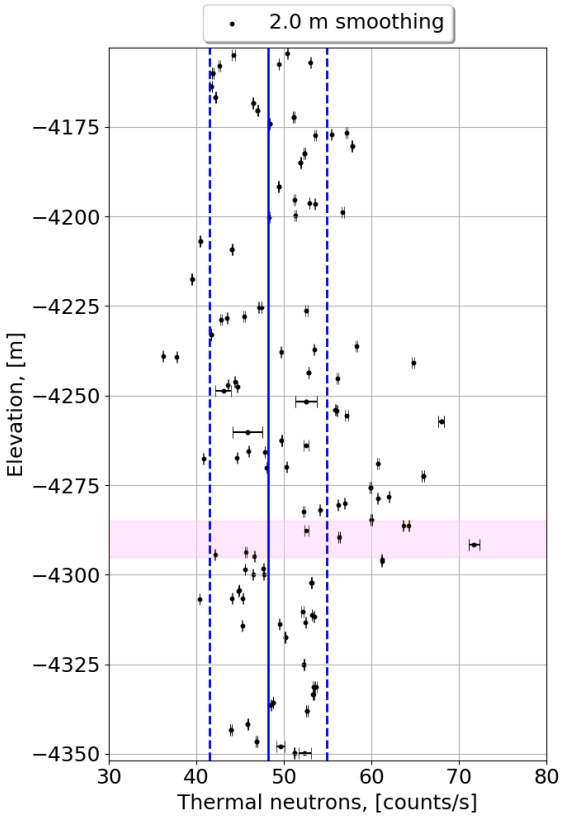

Figure S9: **Thermal neutron count rates from DAN passive measurements**. Thermal neutrons (~0.4 eV to <0.1 MeV) count rates are smoothed over 2 meters of elevation with Poisson-distributed uncertainties added in quadrature. The blue solid and dashed lines represent the mean and 1 standard deviation of the plotted data. Thermal neutron counts were computed by subtracting the CETN detector counts, sensitive to less than ~0.4 eV, from the CTN detector counts, sensitive to <0.1 MeV. Data was acquired while Curiosity rover was stationary. The shaded purple bar denotes the elevations where the hydrated Mg-sulfate enriched lithology is observed (Figure 1).

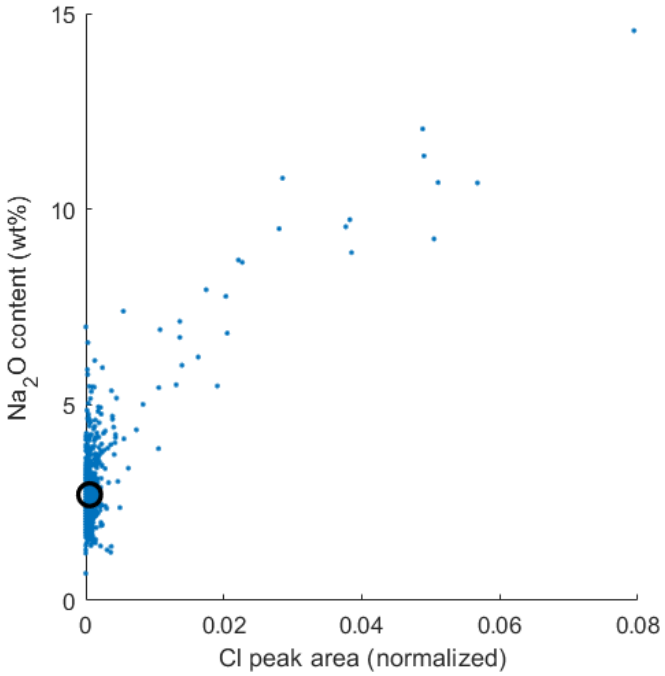

Figure S10: **Na_2O content as a function of Cl peak area for ChemCam Murray bedrock targets.** Cl peak area is obtained by peak fitting at 837.8 nm normalized to total detector intensity (Thomas et al., 2018). This data show that points significantly above the average (black circle) have correlated Cl peak area and Na2O content consistent with halite detections and observed sporadically as isolated points in ChemCam bedrock targets (Thomas et al., 2018).

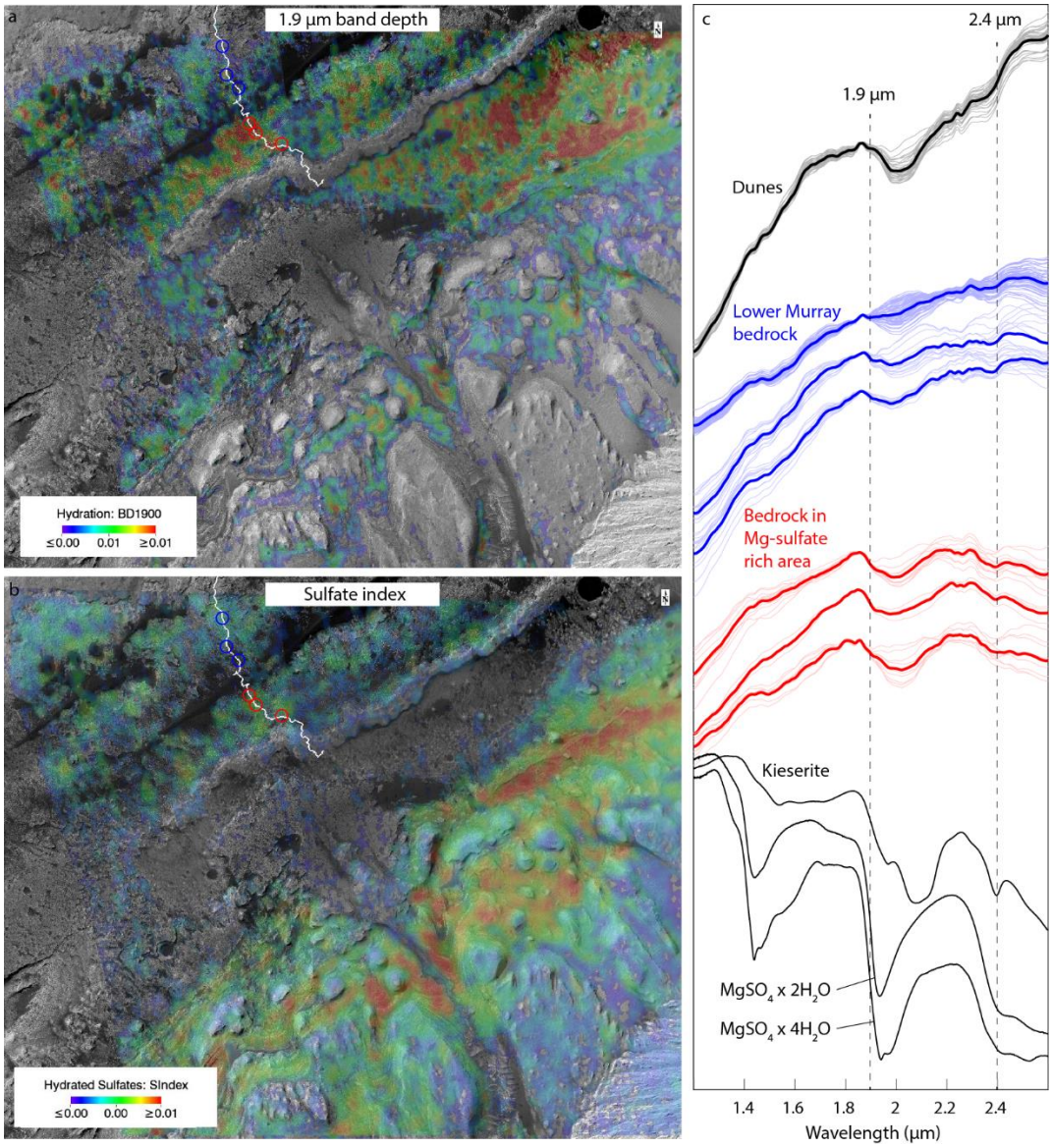

Figure S11: **Hyperspectral orbital data consistent with hydrated sulfate enrichments.** Spectral parameterization and spectral retrievals from CRISM observation FRT0000B6F1 on the slopes of Mt Sharp, with Curiosity's traverse through sol 1950 shown in white. **a**, The absorption depth at 1.9µm, indicative of minerals containing structural OH and H_2O (Clark, 1999). The area just to the north of the anhydrous Vera Rubin Ridge, where Curiosity traverse between Sols 1670-1800, has a moderately enhanced hydration absorption. **b**, Hydrated sulfate minerals are characterized by the presence of a broad asymmetric hydration feature between 1.9 and 2.1 µm and an absorption or shoulder around 2.4 µm due to an overtone of the S-O bend and OH vibrations (Cloutis et al., 2006). The S-Index measures the convexity of the spectrum at 2.29 µm to capture the presence of both these features. In addition to the stratified layers in the middle and upper Mt Sharp units, the area to the north of Vera Rubin ridge has a slightly enhanced SIndex signature. **c**, Spectra collected from the Bagnold Dunes (black), the lower Murray formation (blue, and blue circles in **a** and **b**) and the Mg-sulfate enriched region (red, and red circles in **a** and **b**), compared to laboratory spectra of Mg-sulfates of varying hydration, courtesy Alian Wang at Washington University in St Louis. The mean spectrum from each defined region is shown in bold, and spectra are normalized to the mean value at 1.9 µm to allow more explicit comparison. Spectra from the lower Murray formation and the Bagnold dunes are less consistent with a hydrated Mg-sulfate component.

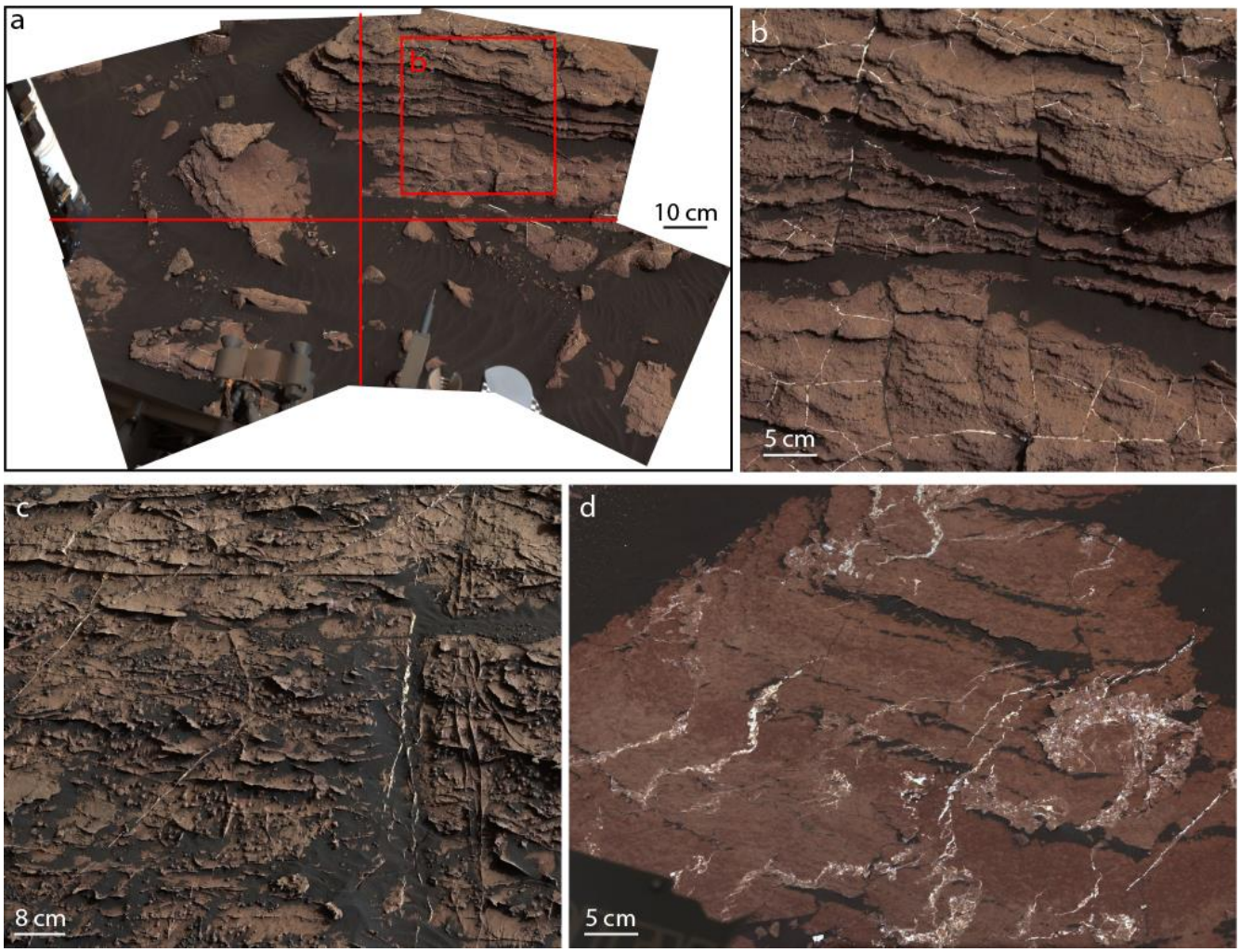

Figure S12: **Examples of Ca-sulfate veins as mapped in the Murray formation**. **a**, Example of MastCam M32 workspace mosaic of Murray bedrock (mcam0738), separated in 4 quadrants (red lines). Workspace mosaics always consist of MastCam M32 image tiles covering the surface directly in front the rover (at ~2 to 4 m distance from the rover mast). For each quadrant the presence of veins is evaluated, and quadrants where bedrock or blocks of bedrock comprise less than a quarter of the image are rejected. **b**, Close up on the upper right quadrant on mosaic (**a**), showing an example of a high-density presence of vertical Ca-sulfate veins. **c**, Example of a mosaic with bedrock including high density of both horizontal and vertical veins (mcam09306). **d**, Example of bedrock showing a high-density of subhorizontal veins (mcam08521).

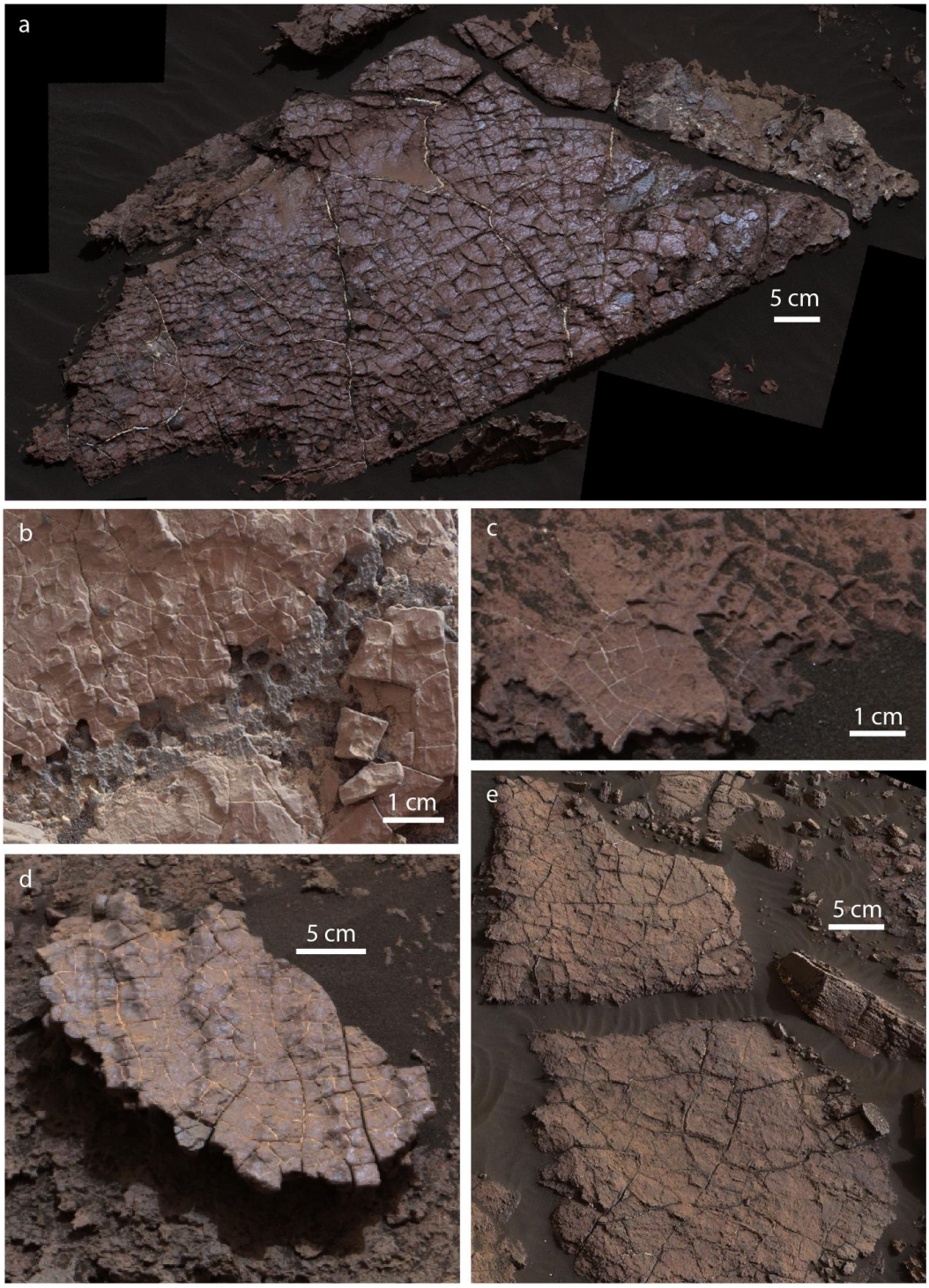

Figure S13: **Examples of putative desiccation cracks in the Murray fm.** Each image contains ridges that form polygonal networks with T-junctions and continuous arcuate shapes, and appear to correspond to fractures that penetrate the underlying bed. These images are at a spatial scale where it is difficult to determine whether the fractures were filled with sediment, an important criterion for positively identifying desiccation cracks. a, For reference Old Soaker mudcracks described in Stein et al. (2018), MAHLI Morancy Cove 25 cm standoff, Sol 1668; b, MR_mcam07473, Sol 1487; c, MR_mcam07472, Sol 1487; d, MR_mcam07441, Sol 1482; e, ML_mcam07401 Sol 1475.

Sample set	Reference	Amount of sulfate in mixture (wt%)
K1919 and hematite + Mg-sulfate	this study	0, 1, 5, 10, 15, 20, 25, 30, 40, 70, 100
K1919 + Mg-sulfate	Anderson et al. (2017)	0, 0.5, 5, 10, 30, 50, 70, 100
K1919 + Ca-sulfate	Anderson et al. (2017)	0, 0.5, 5, 10, 30, 50, 70, 100

Table S3: **Sample sets used for acquisition of laboratory data.** Samples of Mg-sulfates mixed with K1919 basalt doped with 7 wt% hematite were produced for this study to better resolve the variation of the sulfur signal in the 10-50 wt% added sulfate range (Figure S2). Composition of the K1919 basalt powder used are reported in Anderson et al. (2017). The K1919 doped with 7 wt% hematite better represent the iron content of typical Martian basalts and was produced to test the robustness of the sulfur analysis with different matrices.

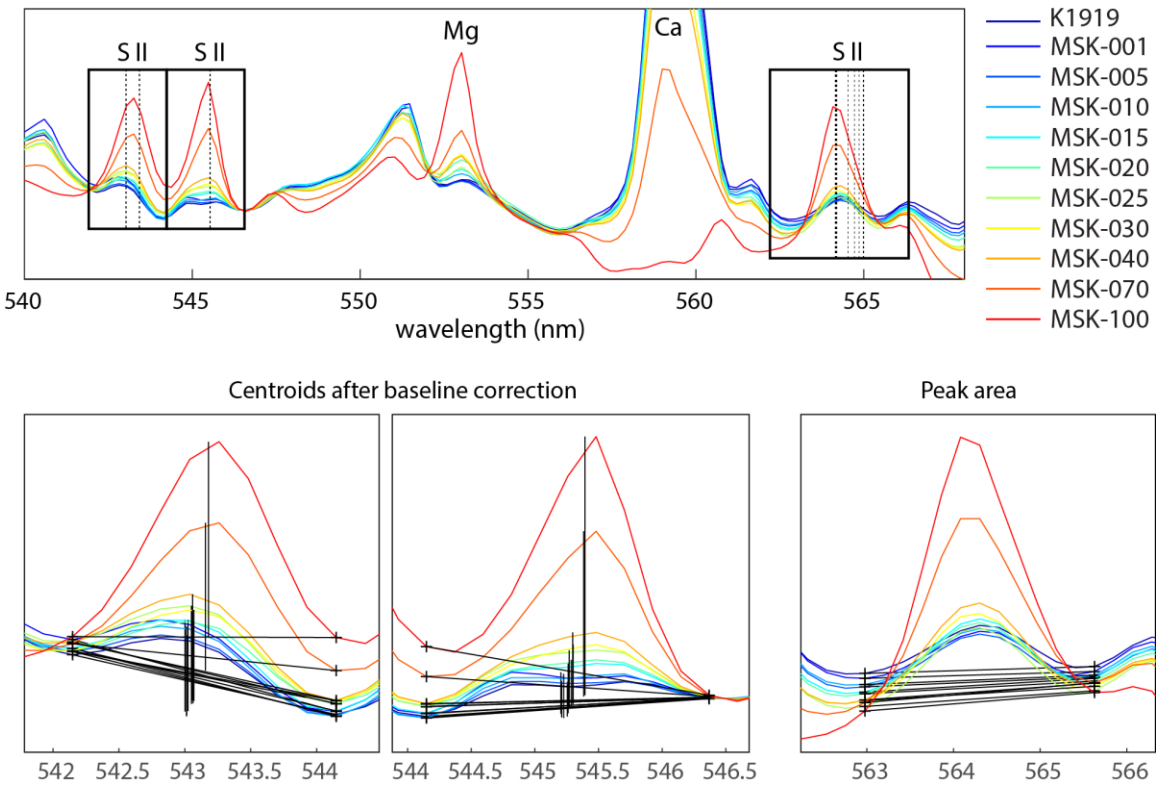

Figure S14: **Laboratory reference spectra of S emission peaks.** Top: average laboratory spectra in the region of the sulfur emission peaks (vertical dotted lines) for each Mg-sulfate-basalt pellet mixtures, with close-ups (boxes) on areas of useful signal. Bottom: centroid location for each spectra (black vertical lines) for peaks at ~543 nm and ~545.5 nm, and peak area at ~564 nm, after baseline correction (black segments).

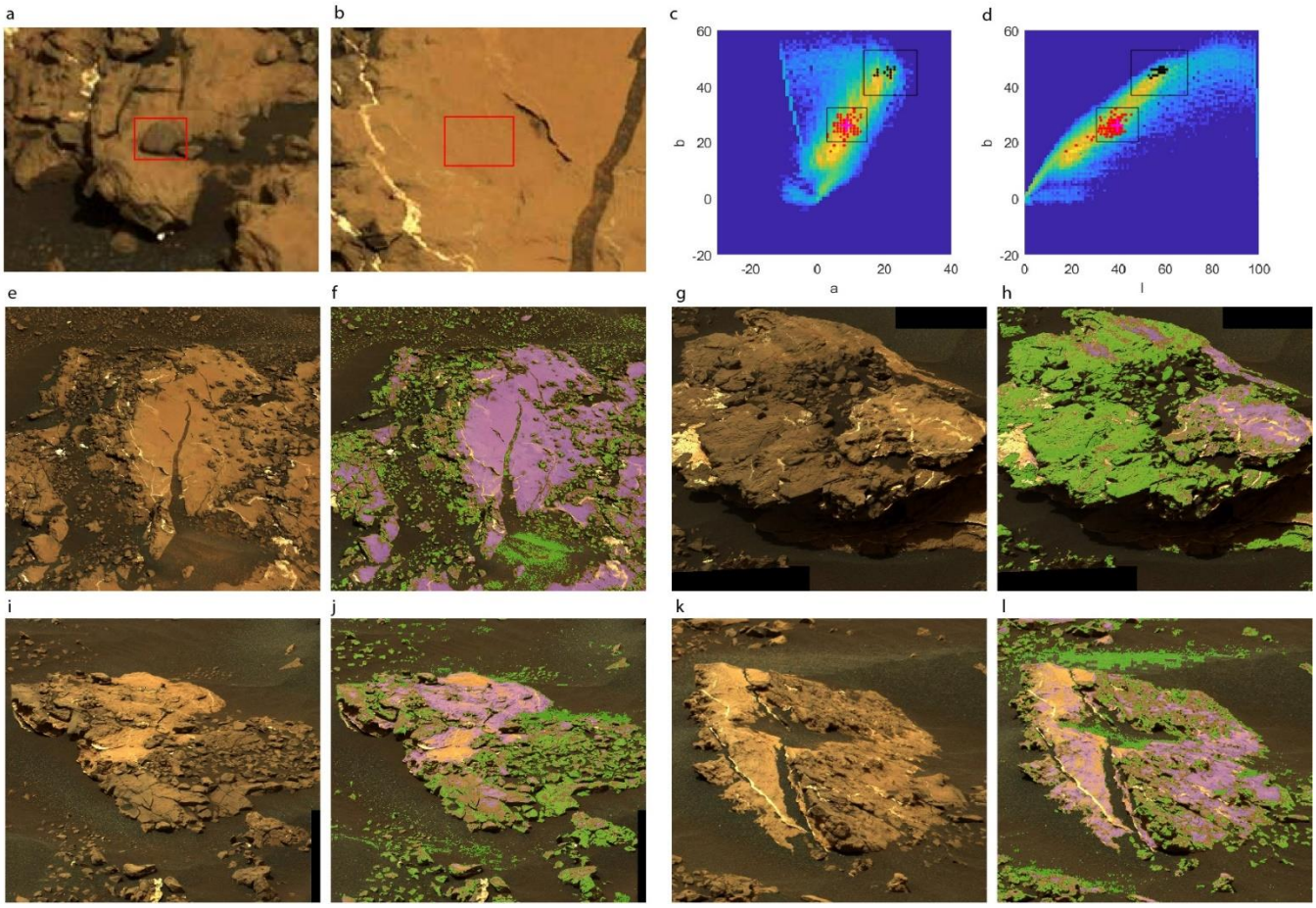

Figure S15: **Color mapping on radiometrically corrected MastCam images. a-b**, highlighted with red rectangles: image of ChemCam target Norwood Cove rock fragment with homogeneous Mg-sulfate enrichment, and nearby typical Murray bedrock (MLF_546550938RAD_S0622248MCAM08716M2). **c-d**, CIE L*a*b* parameter density plots of the MastCam image with corresponding parameter intervals (rectangles) for the Norwood Cove fragment (red dots) and Murray bedrock (dark dots). **e-l**, other images where Mg-sulfate enriched lithology is observed with maps corresponding to the Norwood Cove fragment (green overlay) and Murray bedrock (blue overlay). **e-f**, mcam08716. **g-h**, mcam08707. **i-l**, mcam08708.

Additionnal references :

Anderson, D. E., Ehlmann, B. L., Forni, O., Clegg, S. M., Cousin, A., Thomas, N. H., et al. (2017). Characterization of LIBS emission lines for the identification of chlorides, carbonates, and sulfates in salt/basalt mixtures for the application to MSL ChemCam data. *Journal of Geophysical Research: Planets*, *122*(4), 744–770. https://doi.org/10.1002/2016JE005164

Berger, J. A., Schmidt, M. E., Gellert, R., Campbell, J. L., King, P. L., Flemming, R. L., et al. (2016). A global Mars dust composition refined by the Alpha-Particle X-ray Spectrometer in Gale Crater. *Geophysical Research Letters*, *43*(1), 67–75. https://doi.org/10.1002/2015GL066675

Clark, R. N. (1999). Spectroscopy of rocks and minerals, and principles of spectroscopy. *Manual of Remote Sensing*, *3*(3–58), 2–2.

Clegg, S. M., Wiens, R. C., Anderson, R., Forni, O., Frydenvang, J., Lasue, J., et al. (2017). Recalibration of the Mars Science Laboratory ChemCam instrument with an expanded geochemical database. *Spectrochimica Acta Part B: Atomic Spectroscopy*, *129*, 64–85. https://doi.org/10.1016/j.sab.2016.12.003

Cloutis, E. A., Hawthorne, F. C., Mertzman, S. A., Krenn, K., Craig, M. A., Marcino, D., et al. (2006). Detection and discrimination of sulfate minerals using reflectance spectroscopy. *Icarus*, *184*(1), 121–157.

Maurice, S., Clegg, S. M., Wiens, R. C., Gasnault, O., Rapin, W., Forni, O., et al. (2016). ChemCam activities and discoveries during the nominal mission of the Mars Science Laboratory in Gale crater, Mars. *Journal of Analytical Atomic Spectrometry*, *31*, 863–889. https://doi.org/10.1039/C5JA00417A

Rapin, W., Meslin, P.-Y., Maurice, S., Wiens, R. C., Laporte, D., Chauviré, B., et al. (2017). Quantification of water content by laser induced breakdown spectroscopy on Mars. *Spectrochimica Acta Part B: Atomic Spectroscopy*, *130*, 82–100. https://doi.org/10.1016/j.sab.2017.02.007

Stein, N., Grotzinger, J. P., Schieber, J., Mangold, N., Hallet, B., Newsom, H., et al. (2018). Desiccation cracks provide evidence of lake drying on Mars, Sutton Island member, Murray formation, Gale Crater. *Geology*, *46*(6), 515–518. https://doi.org/10.1130/G40005.1

Thomas, N. H., Ehlmann, B. L., Meslin, P.-Y., Cousin, A., Forni, O., Rapin, W., et al. (2018). MSL ChemCam Observations of Chloride Salts in Gale Crater, Mars (Vol. 49, p. 2876). Presented at the LPSC. Retrieved from http://adsabs.harvard.edu/abs/2018LPI....49.2876T